

Hybrid-Filler-Incorporated, Photocurable, Thermally Conductive Elastomers with High Stretchability and Self-Attachability

Jong-Ho Back, Wonjoo Lee, Hyun-Joong Kim, Youngchang Yu,* and Dowon Ahn*



Cite This: *Ind. Eng. Chem. Res.* 2023, 62, 9257–9267



Read Online

ACCESS |



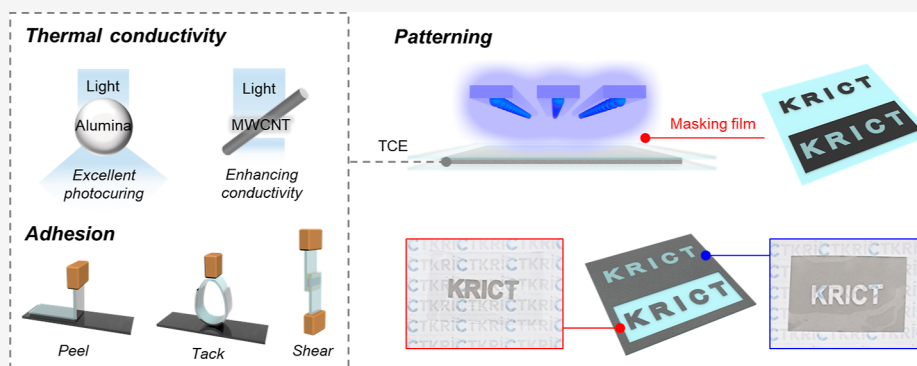
Metrics & More



Article Recommendations



Supporting Information



ABSTRACT: The thermal management issues caused by low-thermal-conductivity elastomers in flexible devices can be mitigated using thermally conductive elastomers (TCEs), which contain thermally conductive fillers. TCEs are usually prepared by solvent mixing and thermal curing, but these steps are also problematic as they emit volatile organic compounds and cause thermal damage, respectively. Furthermore, fabrication of a complex structure is strictly restricted in these steps. Therefore, we fabricated a TCE by photocuring and additionally imparting adhesive properties, enabling uniform heat transfer. White spherical alumina and black rod-shaped multiwalled carbon nanotubes were used together as a hybrid filler. The prepared TCE exhibited higher adhesive strength than a commercial TCE, especially in terms of its lap shear strength, which was 61.5-fold higher. Grid-patterned TCEs were successfully manufactured by photocuring with a masking film. This patterning can facilitate the fabrication of complex-structured TCEs by light-driven three-dimensional printing.

1. INTRODUCTION

Elastomers are essential for soft devices, such as wearable electronics,^{1–3} stretchable electronics,^{4–6} and soft robotics.^{7–9} However, the low thermal conductivity of elastomers impedes thermal management in terms of heat dissipation.¹⁰ Thermally conductive elastomers (TCEs), which comprise elastomeric matrices embedded with thermally conductive fillers, have been employed to address this issue. TCEs are conventionally fabricated by solvent mixing of a matrix and filler,^{11–16} which can emit volatile organic compounds during solvent drying. Thermal curing can be adopted to circumvent the use of solvents, but it can thermally damage the substrate.^{17–19} Photocuring shows remarkable promise as an alternative to solvent mixing and thermal curing because of several advantages, including solvent-free nature, rapid curing, thermal damage-free, cost reduction, and lack of filler sedimentation. In particular, photocuring facilitates the fabrication of complex-structured composites via masking patterns or three-dimensional (3D) printing,^{20,21} which cannot be completely achieved by thermal curing. However, despite these advantages, photocurable TCEs have been rarely studied^{21–23} because thermally conductive fillers typically prevent photocuring.²⁴

Liquid metals,^{12,17–19} graphene,^{25–29} silver nanowires,³⁰ carbon nanotubes (CNTs),^{29,31,32} boron nitride,^{11,22,33} and alumina^{34–36} have all been used as thermally conductive fillers for TCEs. Because fillers must be in contact to achieve pathways for heat transfer, their inherent conductivity and shape are critical to determining the bulk thermal conductivity of the composites.³⁷ At identical filler volume fractions, wire- and rod-type fillers exhibit higher thermal conductivities than spherical fillers because of their high aspect ratios.³⁸ To form efficient conductive pathways, two or more types of fillers, i.e., hybrid fillers, are usually used simultaneously.^{13–16,29,39–45} However, some fillers largely impede light penetration, thereby hindering photocuring. For instance, although black fillers, such as MXenes, graphene, and CNTs, exhibit excellent

Received: March 16, 2023

Revised: May 3, 2023

Accepted: May 22, 2023

Published: June 2, 2023



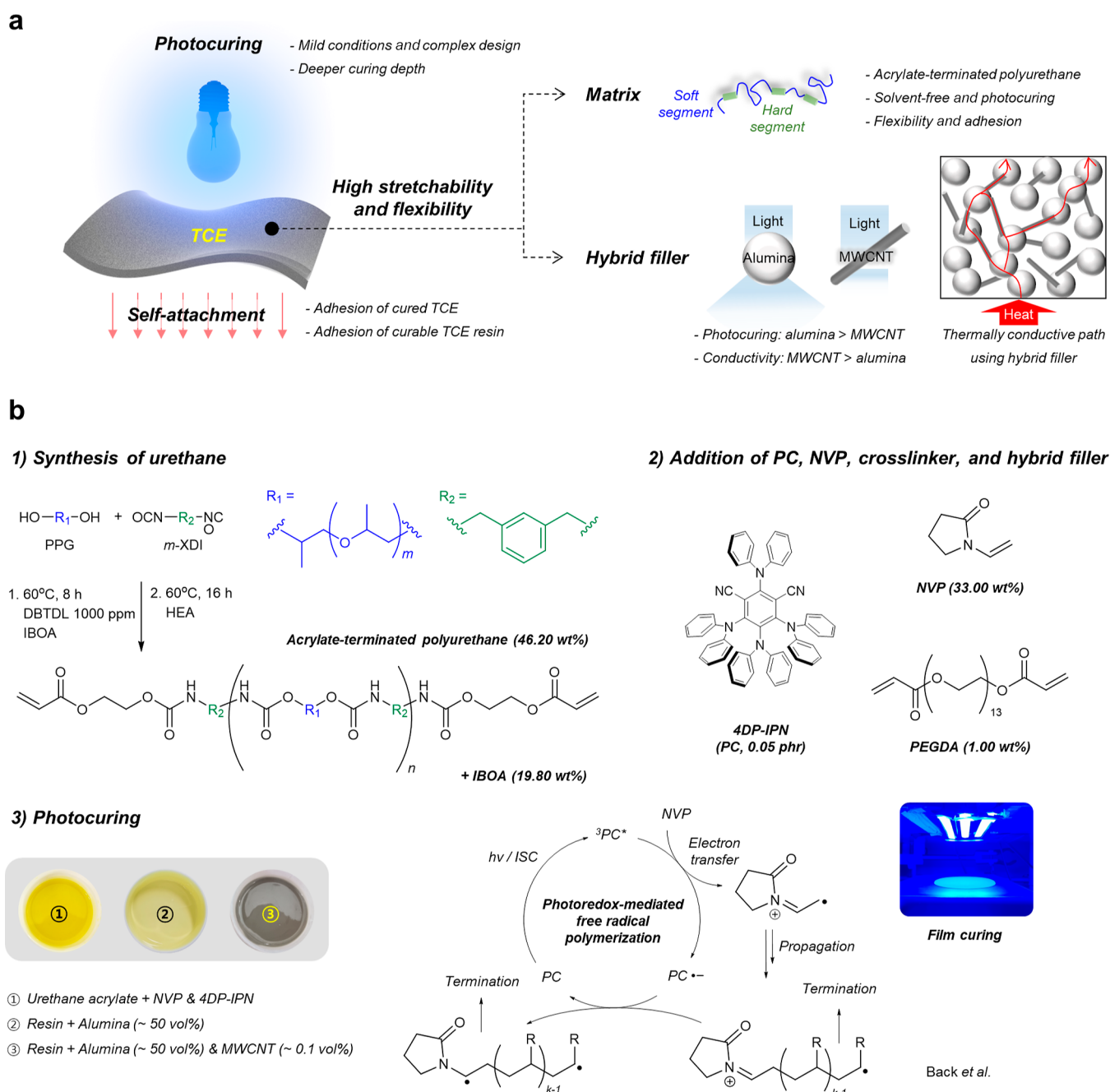


Figure 1. Schematics of the (a) prepared hybrid-filler-incorporated photocurable TCE and the (b) preparation process. The photocuring mechanism has been described elsewhere.⁴⁷

inherent conductivity,^{14–16,29,40–44} they absorb light, which drastically decreases the curing depth with increasing filler loading.⁴⁶ Therefore, photocurable TCEs with optimized filler compositions that can form conductive pathways without significantly impairing the photocuring behavior must be developed.

The fillers added to elastomers affect not only their photocuring behavior but also their stretchability. Specifically, increasing the filler content to improve thermal conductivity decreases stretchability, i.e., the strain limit divided by the Young's modulus. Consequently, overcoming this trade-off by achieving high thermal conductivity while minimizing the loss of stretchability is of considerable interest.^{11,12,17–19,21} Another strategy has been adopted to realize the ultimate goal of

effectively dissipating the heat generated in soft devices composed of TCEs. Imparting a TCE with self-attachability was recently found to establish uniform contact between the TCE and a heat source, which considerably enhanced the heat dissipation.³⁰ This self-attachability characteristic decreased the thermal contact resistance without surface treatment or external pressure, which is particularly useful when the heat source has a rough or curved surface.

Continuing in this vein, this study fabricated a photocurable TCE exhibiting suitable curing behavior, stretchability, thermal conductivity, and self-attachability (Figure 1a). Spherical alumina (Al₂O₃) and rod-shaped multiwalled CNTs (MWCNTs) were simultaneously used as hybrid fillers, with urethane acrylate employed as a self-attachable elastomeric

matrix. The self-attachability of the prepared TCE was adjusted through the monomer composition. The hybrid-filler-containing TCE showed appropriate photocuring behavior and thermal conductivity and maintained a certain level of stretchability. In addition, it exhibited remarkably higher adhesive strength than commercially available TCEs. Finally, patterned TCEs were prepared using a masking film, and their thermal conductivities were compared by thermal imaging.

2. EXPERIMENTAL SECTION

2.1. Materials. **2.1.1. Matrix.** Polypropylene glycol (PPG; $M_n = 2000 \text{ g mol}^{-1}$; Sigma-Aldrich, USA), *m*-xylene diisocyanate (*m*-XDI; Hanwha Solutions, Republic of Korea), and 2-hydroxyethyl acrylate (HEA; Sigma-Aldrich, USA) were used to prepare acrylate-terminated polyurethane (Figure S1). 1-Vinyl-2-pyrrolidinone (NVP; Sigma-Aldrich, USA), isobornyl acrylate (IBOA; Sigma-Aldrich, USA), 4-hydroxybutyl acrylate (HBA; Sigma-Aldrich, USA), and poly(ethylene glycol) diacrylate (PEGDA; $M_n = 700 \text{ g mol}^{-1}$; Sigma-Aldrich, USA) were added to the acrylate-terminated polyurethane to obtain a TCE with an elastomeric matrix. 4DP-IPN, a visible-light-active photocatalyst (PC), was synthesized by following previously reported protocols^{48,49} and used for photopolymerization.

2.1.2. Thermally Conductive Fillers. Spherical alumina particles (DAW-05; Denka, Japan; diameter, $6.4 \mu\text{m}$; true density, 3.96 g cm^{-3}) and rod-shaped MWCNTs (A-Tube-AM97; Applied Carbon Nano Technology, Republic of Korea; diameter, 20 nm ; length, $10 \mu\text{m}$; true density, 1.90 g cm^{-3}) were used as thermally conductive fillers. Scanning electron microscopy (SEM) images of the thermally conductive fillers are shown in Figure S6.

2.1.3. Mixing. 4DP-IPN was first dissolved in NVP to improve solubility, and the 4DP-IPN content in the final TCE resin was fixed at 0.05 phr. To prepare the photocurable TCE resin, dissolved 4DP-IPN, acrylate-terminated polyurethane, and other reactants (NVP, IBOA, HBA, and PEGDA) were mixed to synthesize the elastomer resin, which was subsequently mixed with the thermally conductive fillers. These mixing steps were performed in a paste mixer (ARE-310; Thinky, Japan) under identical conditions (mixing and defoaming: 2000 rpm for 5 and 1 min, respectively).

2.1.4. Curing. The photocurable resins were cured under blue light (450 nm). Specimens for tensile tests, thermal conductivity analysis, 90° peel test, loop tack test, rheometry, and lap shear test were cured with a line-type blue LED for 15 min (distance from LED, 50 mm ; light intensity, 15 mW cm^{-2}). The conversion of the cured TCE can be evaluated by Fourier transform infrared spectrometry, an example of which is shown in Figure S7.

2.2. Characterization. **2.2.1. Curing Depth.** The resin composition used for assessing curing depth is described in Figure S1d. The curing depth was assessed by placing a TCE resin-containing vial 20 mm above a bulb-type blue LED. The light intensity of the LED at this distance was 57 mW cm^{-2} , and the resin was cured for 5 min. After that, the unreacted monomer was removed using acetone. The cured TCE was removed from the vial and dried, and its edges were trimmed. The thickness of the cured TCE core was recorded as the curing depth.

2.2.2. Tensile Tests. The tensile tests were conducted using a universal testing machine (UTM; LS1; AMETEK, USA) with a grip distance and testing speed of 20 mm and 1 mm s^{-1} ,

respectively. Tensile strain was calculated by dividing the machine extension by the length of the narrow part of dumbbell-shaped specimens (12 mm). Stress was calculated by dividing the measured force by the cross-sectional area of the narrow part. Young's modulus was estimated as the slope at 30% strain in the stress–strain curves. The tensile tests were repeated five times for each sample.

2.2.3. Thermal Conductivity. Through-plane thermal conductivity (λ) was estimated as follows

$$\lambda(T) = \alpha(T) \cdot C_p(T) \cdot \rho(T)$$

where α , C_p , ρ , and T represent thermal diffusivity, specific heat capacity, density, and the test temperature, respectively. Specimens were prepared similar to those for the tensile tests and analyzed at 25°C . Density, specific heat capacity, and thermal diffusivity were measured using an electronic densimeter (MD-300S; Alfa Mirage, Japan), differential scanning calorimeter (DSC 25; TA Instruments, USA; N_2 atmosphere, constant heating rate of 5°C min^{-1}), and an LFA 447 NanoFlash device (NETZSCH, Germany), respectively. The thermal conductivity tests were repeated three times for each sample.

2.2.4. 90° Peel Tests. The TCE resin was coated on a $50 \mu\text{m}$ -thick polyethylene terephthalate (PET) film and covered with a release film. The cured films were cut to a width of 10 mm and attached to a stainless-steel substrate (SUS 304) using a 2 kg roller. The resulting specimens were stored at room temperature for 24 h, and the 90° peel tests were conducted using a UTM (LS1, AMETEK, USA) with a testing speed of 5 mm s^{-1} and a peeling angle of 90° . Peel strength was estimated as the average of the debonding force in the 20%–80% range of the working distance. The 90° peel tests were repeated four times for each sample.

2.2.5. Loop Tack Tests. Test specimens for the loop tack tests were prepared similar to those for the 90° peel tests. The two ends of 10 mm -wide, 100 mm -long cured films were tied together to form a loop. The specimen loop was then fixed to the moving clamp of the UTM (LS1; AMETEK, USA) and attached to the substrate (SUS 304) by approaching it to a distance of 10 mm . The attached loop was immediately detached, and the debonding force was recorded. The approaching and debonding test speeds were 5 mm s^{-1} , and the work of adhesion was estimated as the area under the obtained force–extension curve. The loop tack tests were repeated four times for each sample.

2.2.6. Rheometry. Specimens for rheometry were prepared by curing and laminating films. Each laminated film was cut to a diameter of 20 mm , and the storage (G') and loss modulus (G'') were measured using a rheometer (Discovery HR20; TA Instruments, USA) at 25°C with a disposable aluminum plate ($\phi 20 \text{ mm}$). Each sample was analyzed once in these experiments.

2.2.7. Lap Shear Tests. The preparation of specimens for lap shear tests is described in Figure S4. These tests were conducted using the UTM (LS1; AMETEK, USA) at a testing speed of 1 mm min^{-1} , and shear strength was obtained by dividing the applied force by adhesion area ($25 \text{ mm} \times 10 \text{ mm}$). Lap shear strength was estimated as the maximum shear stress required for adhesive fracture. These tests were repeated four times for each sample.

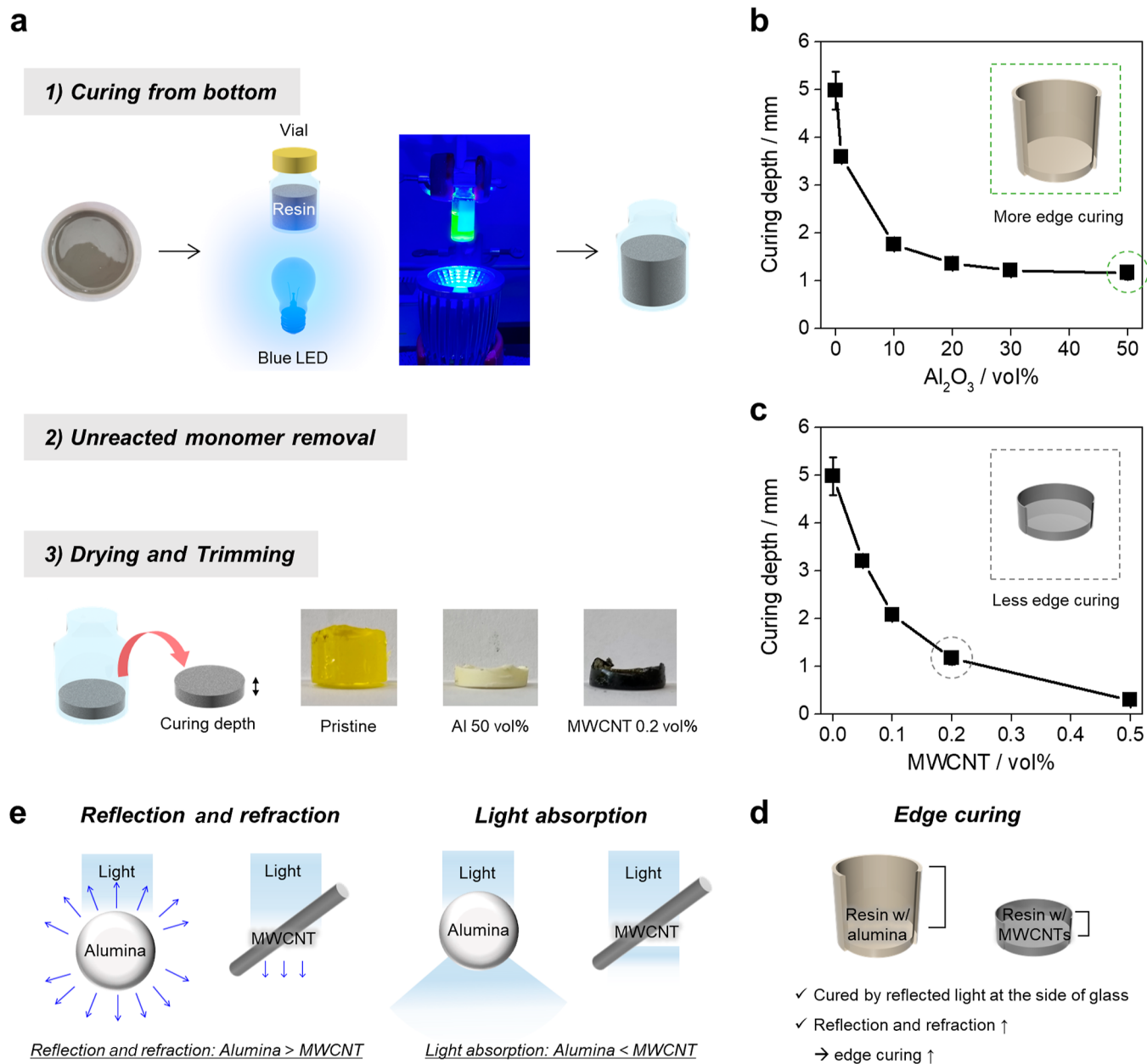


Figure 2. (a) Evaluating the curing depth of fabricated TCEs. Variations in curing depth with different contents of (b) alumina and (c) MWCNTs. (d) Example of edge curing in a TCE with alumina and MWCNTs. (e) Reflection, refraction, and light absorption by alumina and MWCNTs.

3. RESULTS AND DISCUSSION

3.1. Strategy. A photocurable TCE exhibiting stretchability and self-attachment was designed by considering the matrix, filler, and curing depth.

First, urethane acrylate was selected as the TCE matrix because of its photocuring, stretchability, and adhesive properties. Polypropylene glycol (PPG) and *m*-xylene diisocyanate (*m*-XDI) were used as the soft and hard segments of urethane, respectively (Figure 1b); the former makes a composite soft and sticky to enable self-attachability, whereas the latter permits elastic recovery of the composite after stretching. The chain ends of the urethane oligomer were functionalized with acrylate to cure the resin via photoinduced radical polymerization.

Second, alumina and MWCNTs were used together as a hybrid filler. Unlike black MWCNTs, the white alumina was

anticipated to facilitate photocuring. However, at identical filler volume fractions, the rod-shaped MWCNTs provide higher thermal conductivity than spherical alumina because of their higher aspect ratio, which enables them to more efficiently provide heat conduction pathways. Therefore, both fillers were used in a hybrid form to resolve the trade-off between photocuring and thermal conductivity. Metal-based high-aspect-ratio fillers, such as copper and silver nanowires, were not considered because they easily oxidize in air and water.^{50,51}

Third, the TCE was cured by photoinduced radical polymerization using visible light. Although ultraviolet light is predominantly used for photocuring, visible-light curing offers several advantages such as radiation safety,^{52,53} lack of ozone, and greater penetration depths.⁵⁴ Our group has previously polymerized acrylate monomers under blue light (455 nm) by additive-free visible-light-driven photocatalytic polymerization. The kinetics significantly improved with increasing content of

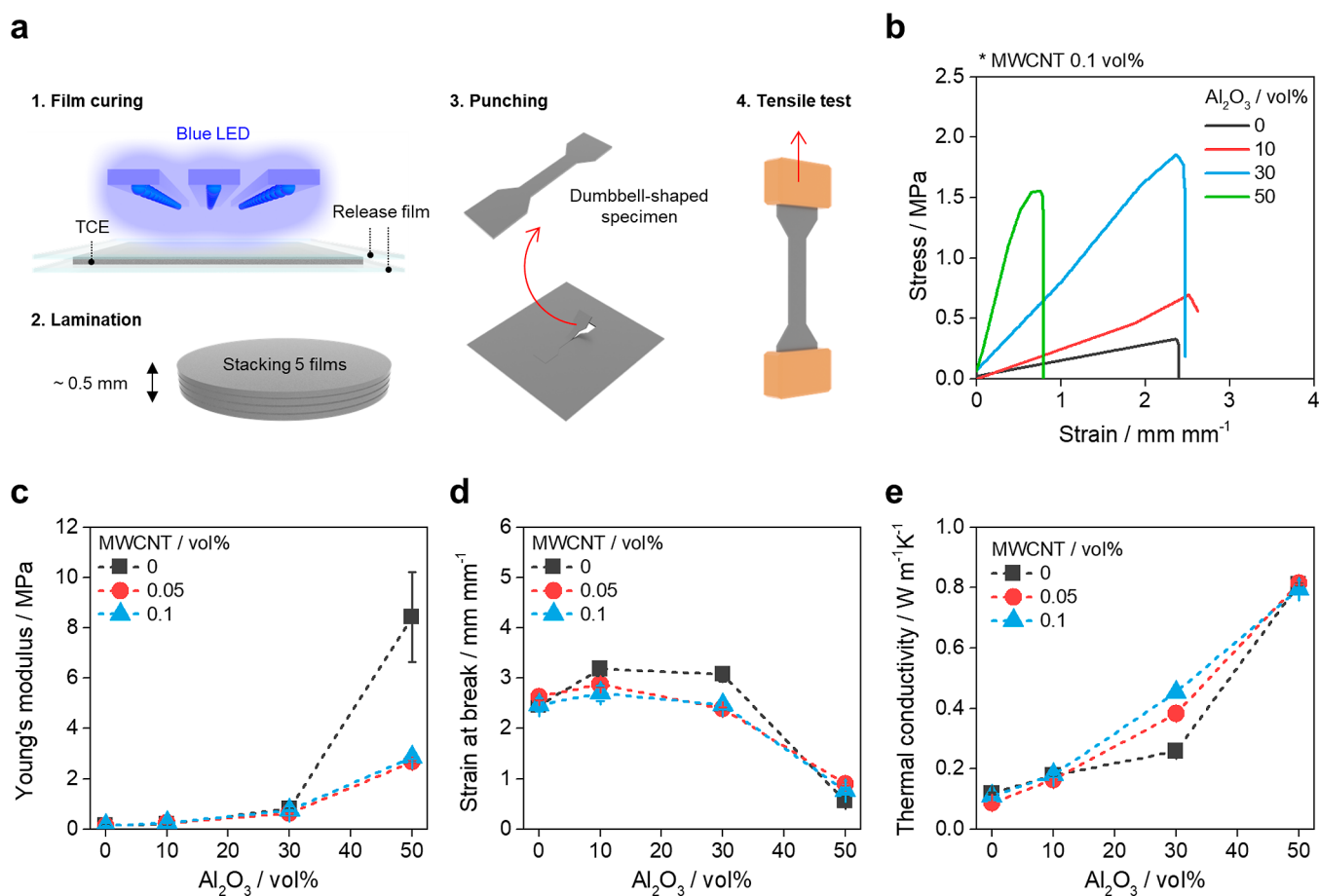


Figure 3. a) Schematic showing the preparation and tensile tests of the photocurable TCEs; the resin composition is detailed in Figure S1. (b) Representative stress–strain curves of photocurable TCEs with different alumina loadings. (c) Young's modulus and (d) strain at break (tensile test results) and (e) through-plane thermal conductivity of photocurable TCEs with different contents of alumina and MWCNTs.

the *N*-vinyl-based monomer, i.e., a boosting monomer (Figure 1b).⁴⁷ 4DP-IPN and NVP were employed as the PC and boosting monomer, respectively. Additionally, NVP played an important role in improving the dispersion of MWCNTs, which can significantly affect the thermal and mechanical properties of the final TCEs (Figure S2).

3.2. Curing Depth. Before preparing and characterizing the fabricated TCE, the curing depth was investigated to optimize the coating thickness of the photocurable TCE resin, the composition of which is detailed in Figures 1b and S1. The curing depth was determined in three steps (Figure 2a): (1) curing TCE in a glass bottle from below (455 nm, 57 mW cm⁻², 5 min); (2) removing the unreacted monomer using acetone; and (3) determining the core thickness after drying and trimming. Because the filler hindered light penetration, the curing depth of the TCE decreased with increasing filler loading (Figure 2b,c). The curing depth of the TCE containing only MWCNTs decreased more sharply with increasing filler content than that of the TCE containing an equivalent amount of alumina, presumably owing to the significant light absorption of the black MWCNTs (Figure 2e). The edges were presumably cured by light reflected or refracted at the sides; nonetheless, the alumina composites showed a higher degree of curing at the edges because the MWCNT equivalents. This difference occurred because alumina reflected or refracted light, whereas the MWCNTs absorbed most of the light (Figure 2d,e). The curing depth of the TCE with the highest

filler content (50 vol % alumina and 0.1 vol % MWCNTs) was found to be 0.2 mm.

3.3. Tensile Tests and Thermal Conductivity Analysis.

The tensile properties and thermal conductivity of the TCE were subsequently investigated to optimize the hybrid filler content. To prepare specimens for the tensile tests (Figure 3a), the photocurable TCE resin was coated onto a release film and covered by another release film to prevent oxygen inhibition and subsequently exposed to blue light (455 nm, 15 mW cm⁻², 15 min). The coating thickness was set to 0.1 mm based on the curing depth of 0.2 mm optimized above the highest filler content. To obtain high-precision results, 0.1 mm-thick films were laminated in a five-layer arrangement, which was then punched to prepare dumbbell-shaped specimens.

When the alumina content was below 30 vol %, the Young's modulus increased only slightly, and no significant difference was detected in the strain at break (Figure 3b–d). Conversely, an increase in alumina to 50 vol % drastically increased the modulus and considerably reduced the strain at break. These changes can be attributed to a greater degree of filler–filler contact, which disrupted some of the connectivity of the elastomer matrix, as supported by scanning electron microscopy images of the fracture surface (Figure S3). The influence of alumina content on the tensile properties of the TCE was significant, whereas that of the MWCNT content was comparatively modest. This disparity may be attributed to the considerably lower quantity of MWCNTs (~0.1 vol %)

Table 1. Compositions of Photocurable TCEs, along with Their Reactant Contents, Through-Plane Thermal Conductivity, Young's Modulus, and Strain at Break^a

entry	urethane acrylate (wt %)	IBOA (wt %)	NVP (wt %)	HBA (wt %)	PEGDA (wt %)	thermal conductivity ($\text{W m}^{-1}\text{K}^{-1}$)	Young's modulus (MPa)	strain at break (mm mm^{-1})
1	46.20	19.80	33.00	0	1.0	0.454(± 0.000)	0.743 (± 0.020)	2.469 (± 0.092)
2	43.30	24.75	24.75	6.20	1.0	0.379(± 0.006)	0.689 (± 0.051)	3.261 (± 0.105)
3	43.30	24.80	18.60	12.30	1.0	0.395(± 0.003)	0.606 (± 0.009)	3.167 (± 0.048)
4	43.30	30.90	12.40	12.40	1.0	0.386(± 0.000)	0.564 (± 0.044)	3.415 (± 0.098)
5	43.50	24.90	24.90	6.20	0.5	0.328(± 0.000)	0.634 (± 0.025)	4.114 (± 0.114)
6	43.75	25.00	25.00	6.25	0	0.342(± 0.001)	0.393 (± 0.066)	6.428 (± 0.280)

^aThe 4DP-IPN content was set at 0.05 wt % with respect to the reactants for all the samples. After preparing the resin, 30 vol % alumina and 0.1 vol % MWCNTs were added.

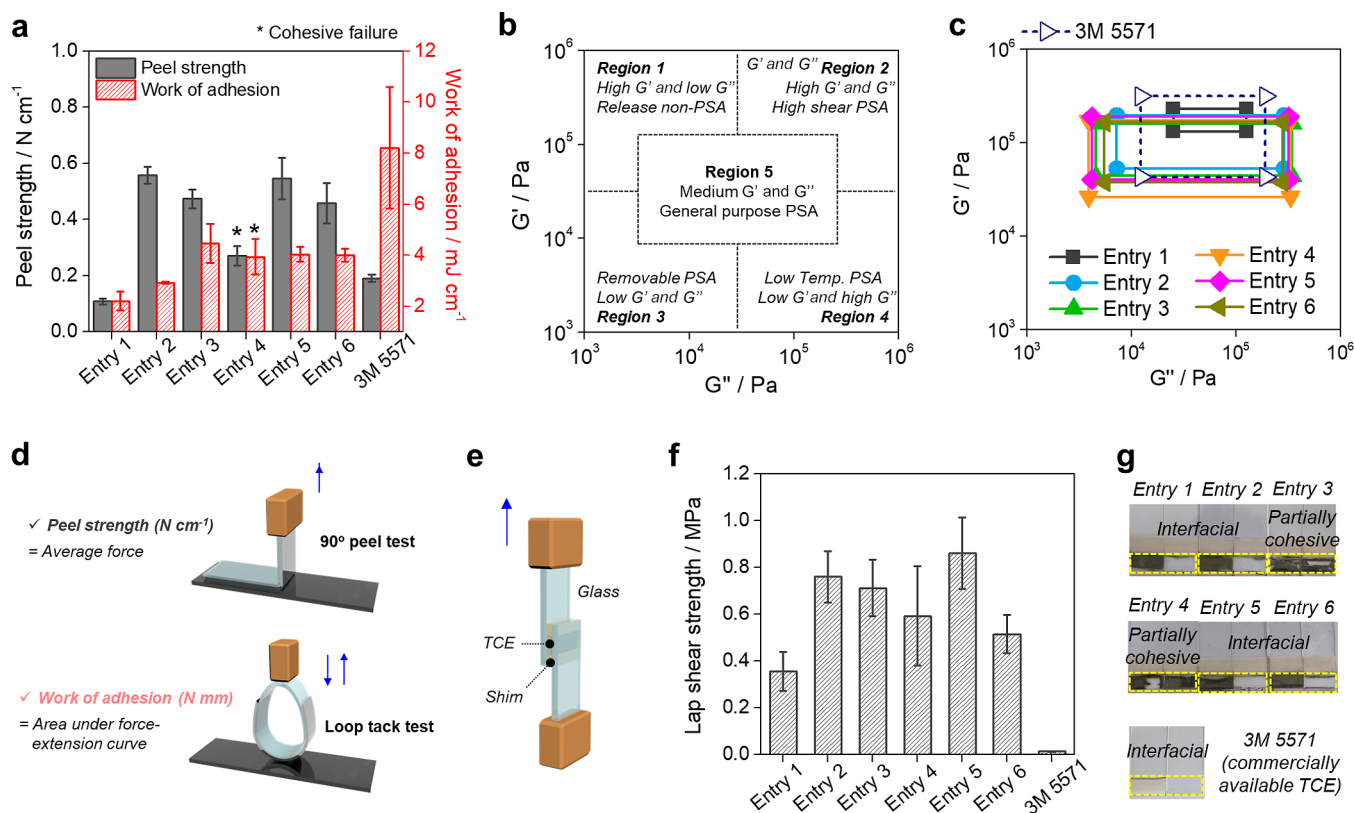


Figure 4. (a) Peel strength and work of adhesion of cured TCEs. (b) General viscoelastic windows of pressure-sensitive adhesives⁵⁵ and (c) viscoelastic window of the fabricated photocurable TCEs. Test schemes for (d) peel strength, work of adhesion, and (e) lap shear strength. (f) Lap shear strengths of photocurable TCE resins. (g) Modes of failure of photocurable TCE resins after the lap shear tests.

present in the composite compared to that of alumina (~50 vol %). Notably, the inclusion of MWCNTs with 50 vol % alumina significantly reduced the modulus of the TCE, which was attributed to the interference of MWCNTs with the contact between alumina particles, thereby establishing sufficient connectivity in the elastomer matrix (Figure S3).

To analyze the thermal conductivity, TCE specimens were prepared similarly to those for the tensile tests but in a disk shape, and they were assessed in the thickness direction. Their thermal conductivity improved with increasing alumina content, and the influence of the MWCNTs was observed only at 30 vol % alumina (Figure 3e). With little (10 vol %) or no alumina, however, the thermal conductivity did not change with increasing MWCNT content, presumably because the overall filler contents were insufficient to form conductive pathways. At 50 vol % alumina, sufficient contact was already achieved between the alumina filler particles even in the

absence of MWCNTs, thereby minimizing the benefits of MWCNTs to the thermal conductivity. Although a TCE with 50 vol % alumina exhibited the highest thermal conductivity among the investigated specimens, its strain at break was excessively low for its application as an elastomer. Therefore, 30 vol % alumina and 0.1 vol % MWCNTs were selected as the optimal hybrid-filler contents to achieve both high strain at break and thermal conductivity.

3.4. Self-Attachment. The matrix composition was also varied to adjust the adhesion properties of the TCE containing the optimized amounts of fillers. Six specimens with different reactant contents were prepared, and the tensile properties of the cured TCEs were first assessed (Table 1). As the amount of the low-molecular-weight crosslinking agent (PEGDA) decreased, the modulus decreased but strain-at-break increased (entries 2, 5, and 6 in Table 1). The other monomers, viz., IBOA, NVP, and HBA, had less effect on the tensile properties

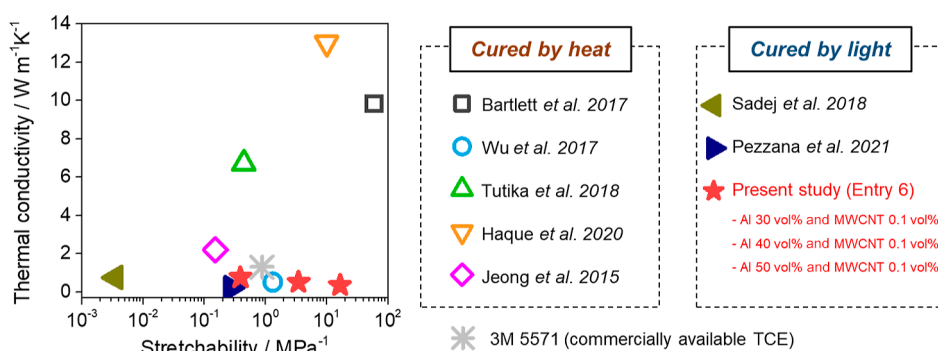


Figure 5. Thermal-conductivity–stretchability data of various TCEs.^{11,12,17–19,21,22} The stretchability of each TCE was calculated by dividing the strain at break (mm mm^{-1}) by the Young's modulus (MPa). The resin composition indicated by a star corresponds to entry 6 in Table 1.

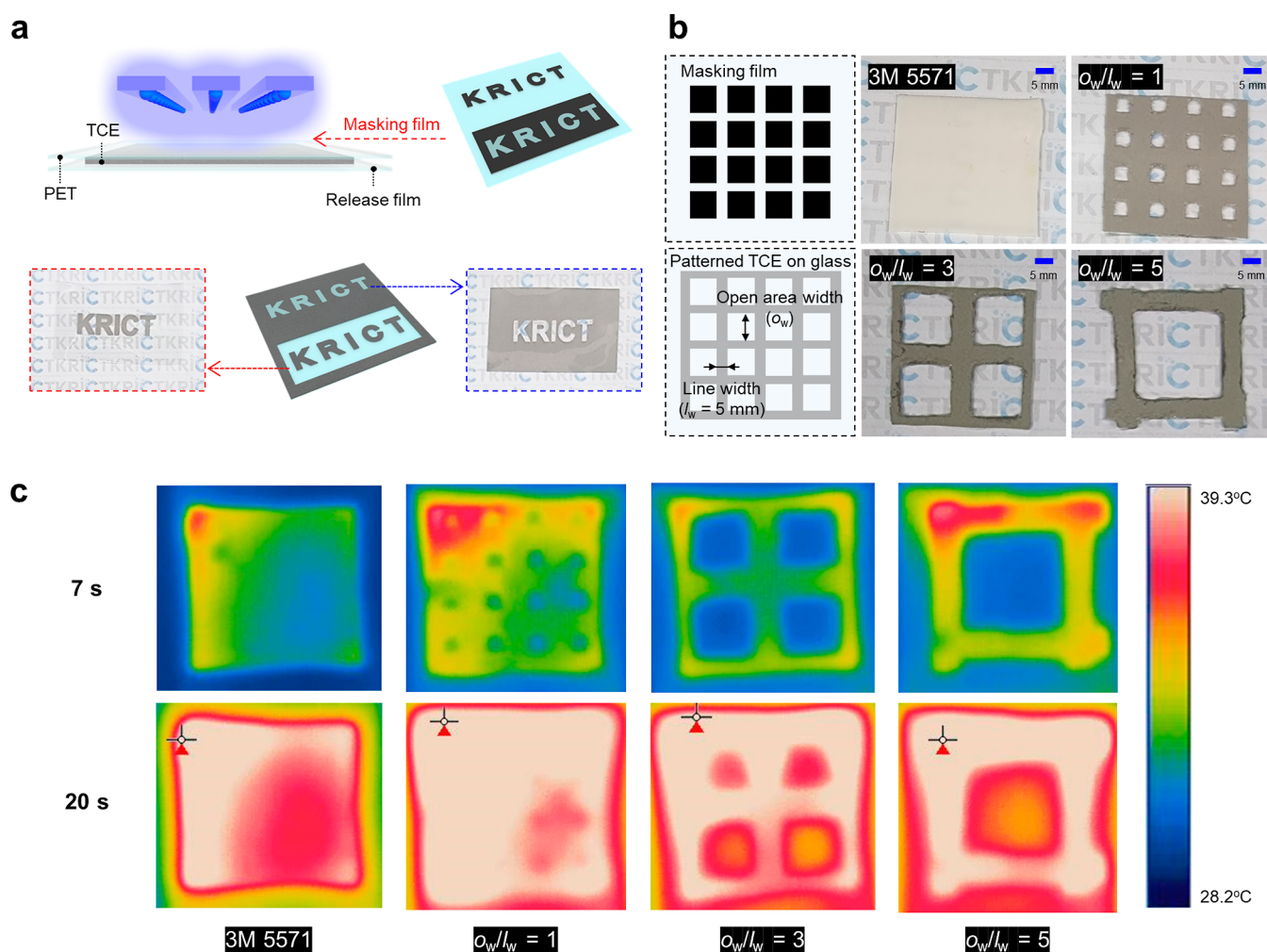


Figure 6. a) Photocuring of the TCE through a patterned masking film (top) and the patterned film obtained after removing the uncured region using acetone (bottom). (b) Fabrication of a grid-patterned TCE using a square-patterned masking film, with schematics of the masking film and the patterned TCE (left) and photographs of three different grid-patterned TCEs and 3 M 5571 (right). (c) Thermal images of a patterned TCE and 3 M 5571 attached to a hot plate that acquired 7 s (top) and 20 s (bottom) after attachment. The sample compositions and manufacturing protocols are detailed in Figure S5.

of the TCE (entries 1, 2, 3, and 4 in Table 1). The thermal conductivities of the prepared TCEs were similar because the alumina and MWCNT contents were fixed at 30 and 0.1 vol %, respectively.

Photocurable TCEs can be attached as pressure-sensitive adhesives (PSAs) or light-curable adhesives. The peel strength and work of adhesion of PSA-type TCEs were assessed by

conducting 90° peel tests and loop tack tests, respectively (Figure 4d). The peel strength indicates the degree of adherence of a PSA to a substrate, and the work of adhesion in the loop tack tests indicates the short-term efficacy of adhesion. The adhesive strengths of the prepared TCEs were compared with that of 3 M 5571, a commercially available TCE with sufficient tack to facilitate pre-assembly. Entry 1, i.e.,

the TCE that exhibited the highest modulus and excluded the interfacial-adhesion-facilitating HBA, showed the lowest peel strength and work of adhesion among the samples (Figure 4a). Entry 4, which was the TCE with the highest content of the monomer with a low glass-transition temperature (HBA), exhibited cohesive failure during the 90° peel test and loop tack test because its cohesive strength was lower than its interfacial adhesion strength. Compared with 3 M 5571, however, most of the prepared TCEs exhibited higher peel strengths, although they showed lower work of adhesion values.

Viscoelastic windows are crucial for assessing PSAs because their viscoelasticity considerably affects their wettability and cohesive strength.^{55,56} The physical properties and potential applications of PSAs can be predicted based on the region in which the drawn viscoelastic windows appear (Figure 4b).⁵⁵ Viscoelastic windows are composed of four points derived from the storage and loss moduli (G' and G'' , respectively) at bonding and debonding frequencies (0.01 and 100 Hz, respectively). The viscoelastic windows of the prepared TCEs and 3 M 5571 belonged to region 5, suggesting that the prepared TCEs were suitable as general-purpose PSAs in terms of G' and G'' (Figure 4c).

Meanwhile, the adhesion strengths of light-curable adhesives are generally assessed based on their lap shear strengths.^{47,57,58} To test this property, specimens were prepared by sandwiching the photocurable TCE resin between two glass slides, followed by curing under blue light (Figures 4e and S4). The lap shear strengths of all prepared TCEs (Figure 4f) were higher than those of 3 M 5571 (0.014 MPa) and conventional photo-responsive acrylic adhesives (0.150–0.341 MPa).^{47,57,58} Specifically, the highest lap shear strength (0.861 MPa) was 61.5 times greater than that of 3 M 5571. Increasing the HBA content enhanced the TCE–substrate interfacial adhesion (Figure 4a,f); however, an exceedingly high HBA content reduced the cohesiveness, leading to cohesive failure in adhesion tests (Figure 4a,g).

3.5. Fabrication of Complex-Structured TCEs. Before fabricating a complex structure from the photocurable TCE, the balance of thermal conductivity and stretchability of previously reported specimens was compared with that of the TCE optimized in this study (Figure 5). Thermally curable TCEs containing liquid metals as conductive fillers^{12,17–19} generally exhibit higher stretchability and thermal conductivity than photocurable TCEs^{21,22} because higher filler contents can be added to the former. Notably, the stretchability and thermal conductivity of the optimal photocurable TCE reported herein were higher than those of previously reported photocurable TCEs and comparable to those of a commercially available TCE (3 M 5571) and some previously reported thermally curable TCEs.¹¹

Among the various advantages of curing TCEs using light instead of heat, the most significant one is the possibility of fabricating complex-structured TCEs. To demonstrate the feasibility of constructing photocurable TCEs in a complex structure, patterned masking film was employed (Figure 6a). Specifically, grid-patterned TCEs were obtained using a square-patterned masking film, and various films were prepared with different ratios of the open area width (o_w) and line width (l_w) (Figure 6b). The thermal conductivity of the patterned TCEs was assessed by monitoring the heat transferred from a 50 °C hot plate (Figure S5). Thermal imaging revealed that heat was transferred along the lines of the patterned TCE, and

the level of heat transfer along the patterned lines was similar to that of commercially available TCEs (Figure 6c).

Therefore, a patterned TCE with excellent heat-transfer characteristics was fabricated, and the patterning of this TCE could be utilized to manufacture advanced devices that require stretchable, self-attachable, and complex-structured TCEs. However, limitations such as difficulties in making the patterned lines thinner and poor resolution exist. These issues, which possibly occurred during manual removal of the uncured region (Figure S5), could be easily addressed by more advanced light-driven 3D-printing technology.

4. CONCLUSIONS

Photocurable TCEs were successfully prepared, and their curing depth, tensile properties, thermal conductivity, and adhesive properties were assessed. Spherical alumina and rod-shaped MWCNTs were used simultaneously as a hybrid filler for the TCEs. Increasing the alumina content resulted in both greater curing depth and improved thermal conductivity. Additionally, the MWCNTs further enhanced thermal conductivity at 30 vol % alumina, albeit with a significantly lower curing depth. The composition of acrylate-terminated polyurethane, which was used as the photocurable matrix, was also varied to adjust the tensile and adhesive properties. The excellent thermal conductivity and stretchability of the prepared TCE (0.50 W m⁻¹ K⁻¹ and 3.47 MPa⁻¹, respectively) were comparable to those of a commercially available TCE (3 M 5571; 1.30 W m⁻¹ K⁻¹ and 0.88 MPa⁻¹, respectively). The self-attachability of the TCE was assessed by employing it as a PSA and light-curable resin. For PSA-type TCEs, most of the prepared TCEs exhibited higher peel strengths (0.27–0.56 N cm⁻¹) than 3 M 5571 (0.19 N cm⁻¹). Lap shear tests were used to assess the adhesive strength of the light-curable resin-type TCEs, which showed a lap shear strength that was up to 61.5 times higher than that of 3 M 5571. Finally, a grid-patterned TCE was successfully prepared using a masking film, which suggested that thinner and more complex TCE designs could feasibly be realized by light-driven 3D printing. The TCE patterning reported herein will be particularly useful in specialized devices that require TCEs with excellent stretchability, attachability, and a complex structure.

■ ASSOCIATED CONTENT

Supporting Information

The Supporting Information is available free of charge at <https://pubs.acs.org/doi/10.1021/acs.iecr.3c00862>.

Synthesis of acrylate-terminated polyurethane, dispersion of MWCNTs, SEM images of the fracture surface, preparation of lap shear test specimens and adhesive strength of commercial tapes, preparation and assessment of grid-patterned TCEs, SEM images of the thermally conductive fillers, and conversion of the thermally conductive elastomer (PDF)

■ AUTHOR INFORMATION

Corresponding Authors

Youngchang Yu – Center for Specialty Chemicals, Korea Research Institute of Chemical Technology, Ulsan 44412, Republic of Korea; Email: ycyu@kriect.re.kr

Down Ahn – Center for Specialty Chemicals, Korea Research Institute of Chemical Technology, Ulsan 44412, Republic of

Korea; orcid.org/0000-0003-4837-0038;
Email: ahndown@kriect.re.kr

Authors

Jong-Ho Back – Center for Specialty Chemicals, Korea Research Institute of Chemical Technology, Ulsan 44412, Republic of Korea; Laboratory of Adhesion & Bio-Composites, Department of Agriculture, Forestry and Bioresources, College of Agriculture and Life Sciences, Seoul National University, Seoul 08826, Republic of Korea; orcid.org/0000-0003-4674-4710

Wonjoo Lee – Center for Specialty Chemicals, Korea Research Institute of Chemical Technology, Ulsan 44412, Republic of Korea

Hyun-Joong Kim – Laboratory of Adhesion & Bio-Composites, Department of Agriculture, Forestry and Bioresources, College of Agriculture and Life Sciences, Seoul National University, Seoul 08826, Republic of Korea; orcid.org/0000-0002-3897-7939

Complete contact information is available at:
<https://pubs.acs.org/10.1021/acs.iecr.3c00862>

Author Contributions

J.-H.B. performed the conceptualization, investigation, and writing the original draft. W.L. participated in the conceptualization and supervision. H.-J.K. executed the methodology and supervision, Y.Y. conducted the methodology and writing—review and editing. D.A. carried out the funding acquisition and writing—review and editing.

Notes

The authors declare no competing financial interest.

ACKNOWLEDGMENTS

This study was supported by the Technology Innovation Program (grant number: 20013963; XDI-related special chemical product manufacturing and high-value-added-material parts application technology development) funded by the Ministry of Trade, Industry, and Energy (MOTIE, Republic of Korea) and supervised by the Korean Research Institute of Chemical Technology (grant number: KS2341-10).

ABBREVIATIONS

TCE	thermally conductive elastomer
MWCNT	multiwalled carbon nanotube
PC	photocatalyst
PPG	polypropylene glycol
<i>m</i> -XDI	<i>m</i> -xylene diisocyanate
HEA	2-hydroxyethyl acrylate
NVP	1-vinyl-2-pyrrolidinone
IBOA	isobornyl acrylate
PEGDA	poly(ethylene glycol) diacrylate
UTM	universal testing machine
PET	polyethylene terephthalate
PSA	pressure-sensitive adhesive
phr	per hundred resin
ISC	intersystem crossing.

REFERENCES

(1) Deng, J.; Kuang, X.; Liu, R.; Ding, W.; Wang, A. C.; Lai, Y. C.; Dong, K.; Wen, Z.; Wang, Y.; Wang, L.; Qi, H. J.; Zhang, T.; Wang, Z. L. Vitriimer elastomer-based jigsaw puzzle-like healable triboelectric nanogenerator for self-powered wearable electronics. *Adv. Mater.* **2018**, *30*, 1705918.

(2) Trung, T. Q.; Ramasundaram, S.; Hwang, B. U.; Lee, N. E. An all-elastomeric transparent and stretchable temperature sensor for body-attachable wearable electronics. *Adv. Mater.* **2016**, *28*, 502–509.

(3) Amjadi, M.; Pichitpajongkit, A.; Lee, S.; Ryu, S.; Park, I. Highly stretchable and sensitive strain sensor based on silver nanowire–elastomer nanocomposite. *ACS Nano* **2014**, *8*, 5154–5163.

(4) Rogers, J. A.; Someya, T.; Huang, Y. Materials and mechanics for stretchable electronics. *Science* **2010**, *327*, 1603–1607.

(5) Stoyanov, H.; Kollosche, M.; Risse, S.; Waché, R.; Kofod, G. Soft conductive elastomer materials for stretchable electronics and voltage controlled artificial muscles. *Adv. Mater.* **2013**, *25*, 578–583.

(6) Sim, K.; Rao, Z.; Ershad, F.; Yu, C. Rubbery electronics fully made of stretchable elastomeric electronic materials. *Adv. Mater.* **2020**, *32*, 1902417.

(7) Markvicka, E. J.; Bartlett, M. D.; Huang, X.; Majidi, C. An autonomously electrically self-healing liquid metal–elastomer composite for robust soft-matter robotics and electronics. *Nat. Mater.* **2018**, *17*, 618–624.

(8) Shian, S.; Bertoldi, K.; Clarke, D. R. Dielectric elastomer based “grippers” for soft robotics. *Adv. Mater.* **2015**, *27*, 6814–6819.

(9) Rich, S. I.; Wood, R. J.; Majidi, C. Untethered soft robotics. *Nat. Electron.* **2018**, *1*, 102–112.

(10) Chen, H.; Ginzburg, V. V.; Yang, J.; Yang, Y.; Liu, W.; Huang, Y.; Du, L.; Chen, B. Thermal conductivity of polymer-based composites: Fundamentals and applications. *Prog. Polym. Sci.* **2016**, *59*, 41–85.

(11) Wu, X.; Yang, Z.; Kuang, W.; Tang, Z.; Guo, B. Coating polyrhodanine onto boron nitride nanosheets for thermally conductive elastomer composites. *Composites, Part A* **2017**, *94*, 77–85.

(12) Haque, A. B. M. T.; Tutika, R.; Byrum, R. L.; Bartlett, M. D. Programmable liquid metal microstructures for multifunctional soft thermal composites. *Adv. Funct. Mater.* **2020**, *30*, 2000832.

(13) Yan, H.; Dai, X.; Ruan, K.; Zhang, S.; Shi, X.; Guo, Y.; Cai, H.; Gu, J. Flexible thermally conductive and electrically insulating silicone rubber composite films with BNNS@ Al₂O₃ fillers. *Adv. Compos. Hybrid Mater.* **2021**, *4*, 36–50.

(14) Song, P.; Liu, B.; Liang, C.; Ruan, K.; Qiu, H.; Ma, Z.; Guo, Y.; Gu, J. Lightweight, flexible cellulose-derived carbon aerogel@ reduced graphene oxide/PDMS composites with outstanding EMI shielding performances and excellent thermal conductivities. *Nano-Micro Lett.* **2021**, *13*, 91.

(15) Guo, Y.; Qiu, H.; Ruan, K.; Wang, S.; Zhang, Y.; Gu, J. Flexible and insulating silicone rubber composites with sandwich structure for thermal management and electromagnetic interference shielding. *Compos. Sci. Technol.* **2022**, *219*, 109253.

(16) Wang, S.; Feng, D.; Guan, H.; Guo, Y.; Liu, X.; Yan, C.; Zhang, L.; Gu, J. Highly efficient thermal conductivity of polydimethylsiloxane composites via introducing “Line-Plane”-like hetero-structured fillers. *Composites, Part A* **2022**, *157*, 106911.

(17) Bartlett, M. D.; Kazem, N.; Powell-Palm, M. J.; Huang, X.; Sun, W.; Malen, J. A.; Majidi, C. High thermal conductivity in soft elastomers with elongated liquid metal inclusions. *Proc. Natl. Acad. Sci. U.S.A.* **2017**, *114*, 2143–2148.

(18) Jeong, S. H.; Chen, S.; Huo, J.; Gamstedt, E. K.; Liu, J.; Zhang, S.-L.; Zhang, Z.-B.; Hjort, K.; Wu, Z. Mechanically stretchable and electrically insulating thermal elastomer composite by liquid alloy droplet embedment. *Sci. Rep.* **2015**, *5*, 18257.

(19) Tutika, R.; Zhou, S. H.; Napolitano, R. E.; Bartlett, M. D. Mechanical and functional tradeoffs in multiphase liquid metal, solid particulate soft composites. *Adv. Funct. Mater.* **2018**, *28*, 1804336.

(20) Ligon, S. C.; Liska, R.; Stampfl, J.; Gurr, M.; Mülhaupt, R. Polymers for 3D printing and customized additive manufacturing. *Chem. Rev.* **2017**, *117*, 10212–10290.

(21) Pezzana, L.; Riccucci, G.; Spriano, S.; Battagazzore, D.; Sangermano, M.; Chiappone, A. 3D Printing of PDMS-Like Polymer Nanocomposites with Enhanced Thermal Conductivity: Boron Nitride Based Photocuring System. *Nanomaterials* **2021**, *11*, 373.

- (22) Sadej, M.; Gojewski, H.; Gajewski, P.; Vancso, G.; Andrzejewska, E. Photocurable acrylate-based composites with enhanced thermal conductivity containing boron and silicon nitrides. *eXPRESS Polym. Lett.* **2018**, *12*, 790–807.
- (23) Wang, S.; Cheng, Y.; Wang, R.; Sun, J.; Gao, L. Highly thermal conductive copper nanowire composites with ultralow loading: toward applications as thermal interface materials. *ACS Appl. Mater. Interfaces* **2014**, *6*, 6481–6486.
- (24) Wang, X.; Feng, Y.; Zhang, L.; Protsak, I.; Jamali, R.; Shu, Y.; Pal, P.; Wang, Z.; Yang, J.; Zhang, D. Fast-cured UV-LED polymer materials filled with high mineral contents as wear-resistant, antibacterial coatings. *Chem. Eng. J.* **2020**, *382*, 122927.
- (25) Sadasivuni, K. K.; Ponnamma, D.; Thomas, S.; Grohens, Y. Evolution from graphite to graphene elastomer composites. *Prog. Polym. Sci.* **2014**, *39*, 749–780.
- (26) Araby, S.; Meng, Q.; Zhang, L.; Kang, H.; Majewski, P.; Tang, Y.; Ma, J. Electrically and thermally conductive elastomer/graphene nanocomposites by solution mixing. *Polymer* **2014**, *55*, 201–210.
- (27) Fang, H.; Zhao, Y.; Zhang, Y.; Ren, Y.; Bai, S.-L. Three-dimensional graphene foam-filled elastomer composites with high thermal and mechanical properties. *ACS Appl. Mater. Interfaces* **2017**, *9*, 26447–26459.
- (28) Zhang, W.; Kong, Q. Q.; Tao, Z.; Wei, J.; Xie, L.; Cui, X.; Chen, C. M. 3D thermally cross-linked graphene aerogel-enhanced silicone rubber elastomer as thermal interface material. *Adv. Mater. Interfaces* **2019**, *6*, 1900147.
- (29) Song, S.; Zhang, Y. Carbon nanotube/reduced graphene oxide hybrid for simultaneously enhancing the thermal conductivity and mechanical properties of styrene-butadiene rubber. *Carbon* **2017**, *123*, 158–167.
- (30) Seong, M.; Hwang, I.; Park, S.; Jang, H.; Choi, G.; Kim, J.; Kim, S. K.; Kim, G. H.; Yeo, J.; Jeong, H. E. Enhanced Thermal Transport across Self-Interfacing van der Waals Contacts in Flexible Thermal Devices. *Adv. Funct. Mater.* **2021**, *31*, 2107023.
- (31) Jo, J. O.; Saha, P.; Kim, N. G.; Chang Ho, C.; Kim, J. K. Development of nanocomposite with epoxidized natural rubber and functionalized multiwalled carbon nanotubes for enhanced thermal conductivity and gas barrier property. *Mater. Des.* **2015**, *83*, 777–785.
- (32) Han, Z.; Fina, A. Thermal conductivity of carbon nanotubes and their polymer nanocomposites: A review. *Prog. Polym. Sci.* **2011**, *36*, 914–944.
- (33) Hong, H.; Jung, Y. H.; Lee, J. S.; Jeong, C.; Kim, J. U.; Lee, S.; Ryu, H.; Kim, H.; Ma, Z.; Kim, T. i. Anisotropic thermal conductive composite by the guided assembly of boron nitride nanosheets for flexible and stretchable electronics. *Adv. Funct. Mater.* **2019**, *29*, 1902575.
- (34) Yang, D.; Huang, S.; Ruan, M.; Li, S.; Yang, J.; Wu, Y.; Guo, W.; Zhang, L. Mussel inspired modification for aluminum oxide/silicone elastomer composites with largely improved thermal conductivity and low dielectric constant. *Ind. Eng. Chem. Res.* **2018**, *57*, 3255–3262.
- (35) Zhang, X.; Maira, B.; Hashimoto, Y.; Wada, T.; Chammingkwan, P.; Thakur, A.; Taniike, T. Selective localization of aluminum oxide at interface and its effect on thermal conductivity in polypropylene/polyolefin elastomer blends. *Composites, Part B* **2019**, *162*, 662–670.
- (36) Benli, S.; Yilmazer, U.; Pekel, F.; Özkar, S. Effect of fillers on thermal and mechanical properties of polyurethane elastomer. *J. Appl. Polym. Sci.* **1998**, *68*, 1057–1065.
- (37) Burger, N.; Laachachi, A.; Ferriol, M.; Lutz, M.; Toniazzo, V.; Ruch, D. Review of thermal conductivity in composites: Mechanisms, parameters and theory. *Prog. Polym. Sci.* **2016**, *61*, 1–28.
- (38) Tao, Y.; Yang, Z.; Lu, X.; Tao, G.; Xia, Y.; Wu, H. Influence of filler morphology on percolation threshold of isotropical conductive adhesives (ICA). *Sci. China: Technol. Sci.* **2012**, *55*, 28–33.
- (39) Yang, G.; Zhang, X.; Pan, D.; Zhang, W.; Shang, Y.; Su, F.; Ji, Y.; Liu, C.; Shen, C. Highly Thermal Conductive Poly (vinyl alcohol) Composites with Oriented Hybrid Networks: Silver Nanowire Bridged Boron Nitride Nanoplatelets. *ACS Appl. Mater. Interfaces* **2021**, *13*, 32286–32294.
- (40) Im, H.; Kim, J. Thermal conductivity of a graphene oxide-carbon nanotube hybrid/epoxy composite. *Carbon* **2012**, *50*, 5429–5440.
- (41) Kholmanov, I.; Kim, J.; Ou, E.; Ruoff, R. S.; Shi, L. Continuous carbon nanotube-ultrathin graphite hybrid foams for increased thermal conductivity and suppressed subcooling in composite phase change materials. *ACS Nano* **2015**, *9*, 11699–11707.
- (42) Li, M.; Sun, Y.; Feng, D.; Ruan, K.; Liu, X.; Gu, J. Thermally conductive polyvinyl alcohol composite films via introducing heterostructured MXene@ silver fillers. *Nano Res.* **2023**, *16*, 7820–7828.
- (43) Zhang, Y.; Ruan, K.; Zhou, K.; Gu, J. Controlled distributed Ti3C2Tx hollow microspheres on thermally conductive polyimide composite films for excellent electromagnetic interference shielding. *Adv. Mater.* **2023**, 2211642.
- (44) Ruan, K.; Gu, J. Ordered alignment of liquid crystalline graphene fluoride for significantly enhancing thermal conductivities of liquid crystalline polyimide composite films. *Macromolecules* **2022**, *55*, 4134–4145.
- (45) Choi, S.; Kim, J. Thermal conductivity of epoxy composites with a binary-particle system of aluminum oxide and aluminum nitride fillers. *Composites, Part B* **2013**, *51*, 140–147.
- (46) Huang, B.; Zhou, Z.; Wei, L.; Song, Q.; Yu, W.; Zhou, Y.; Hu, R.; Zhang, W.; Lu, C. Ti3C2Tx MXene as a novel functional photo blocker for stereolithographic 3D printing of multifunctional gels via Continuous Liquid Interface Production. *Composites, Part B* **2021**, *225*, 109261.
- (47) Back, J.-H.; Kwon, Y.; Roldao, J. C.; Yu, Y.; Kim, H.-J.; Gierschner, J.; Lee, W.; Kwon, M. S. Synthesis of solvent-free acrylic pressure-sensitive adhesives via visible-light-driven photocatalytic radical polymerization without additives. *Green Chem.* **2020**, *22*, 8289–8297.
- (48) Singh, V. K.; Yu, C.; Badgajar, S.; Kim, Y.; Kwon, Y.; Kim, D.; Lee, J.; Akhter, T.; Thangavel, G.; Park, L. S.; Lee, J.; Nandajan, P. C.; Wannemacher, R.; Milián-Medina, B.; Lüer, L.; Kim, K. S.; Gierschner, J.; Kwon, M. S. Highly efficient organic photocatalysts discovered via a computer-aided-design strategy for visible-light-driven atom transfer radical polymerization. *Nat. Catal.* **2018**, *1*, 794–804.
- (49) Song, Y.; Kim, Y.; Noh, Y.; Singh, V. K.; Behera, S. K.; Abudulimu, A.; Chung, K.; Wannemacher, R.; Gierschner, J.; Lüer, L.; Kwon, M. S. Organic Photocatalyst for ppm-Level Visible-Light-Driven Reversible Addition-Fragmentation Chain-Transfer (RAFT) Polymerization with Excellent Oxygen Tolerance. *Macromolecules* **2019**, *52*, 5538–5545.
- (50) Ahn, Y.; Jeong, Y.; Lee, Y. Improved thermal oxidation stability of solution-processable silver nanowire transparent electrode by reduced graphene oxide. *ACS Appl. Mater. Interfaces* **2012**, *4*, 6410–6414.
- (51) Chen, Z.; Ye, S.; Stewart, I. E.; Wiley, B. J. Copper nanowire networks with transparent oxide shells that prevent oxidation without reducing transmittance. *ACS Nano* **2014**, *8*, 9673–9679.
- (52) Ichihashi, M.; Ueda, M.; Budiyo, A.; Bito, T.; Oka, M.; Fukunaga, M.; Tsuru, K.; Horikawa, T. UV-induced skin damage. *Toxicology* **2003**, *189*, 21–39.
- (53) Clydesdale, G. J.; Dandie, G. W.; Muller, H. K. Ultraviolet light induced injury: immunological and inflammatory effects. *Immunol. Cell Biol.* **2001**, *79*, 547–568.
- (54) Elisseeff, J.; Anseth, K.; Sims, D.; McIntosh, W.; Randolph, M.; Langer, R. Transdermal photopolymerization for minimally invasive implantation. *Proc. Natl. Acad. Sci. U.S.A.* **1999**, *96*, 3104–3107.
- (55) Chang, E. Viscoelastic windows of pressure-sensitive adhesives. *J. Adhes.* **1991**, *34*, 189–200.
- (56) Satas, D., *Handbook of Pressure Sensitive Adhesive Technology*. 3rd edition ed.; Satas & Associates: 1999.
- (57) Harper, T.; Slegeris, R.; Pramudya, I.; Chung, H. Single-phase photo-cross-linkable bioinspired adhesive for precise control of adhesion strength. *ACS Appl. Mater. Interfaces* **2017**, *9*, 1830–1839.

(58) Kim, M.; Chung, H. Photo-responsive bio-inspired adhesives: Facile control of adhesion strength via a photocleavable crosslinker. *Polym. Chem.* **2017**, *8*, 6300–6308.

Recommended by ACS

Graphene/Polyolefin Elastomer Films as Thermal Interface Materials with High Thermal Conductivity, Flexibility, and Good Adhesion

Xin Sun, Zheng-Bai Zhao, *et al.*

MARCH 17, 2023
CHEMISTRY OF MATERIALS

READ 

Thermal Interface Materials with High Thermal Conductivity and Low Young's Modulus Using a Solid-Liquid Metal Codoping Strategy

Xu-Dong Zhang, Bing-Yang Cao, *et al.*

JANUARY 05, 2023
ACS APPLIED MATERIALS & INTERFACES

READ 

Positive/Negative Temperature Coefficient Behaviors of Electron Beam-Irradiated Carbon Blacks-Loaded Polyethylene Nanocomposites

Choong-Hee Kim, Soo-Jin Park, *et al.*

DECEMBER 09, 2022
ACS OMEGA

READ 

Size-Controlled Low-Melting-Point-Alloy Particle-Incorporated Transient Liquid-Phase Epoxy Composite Conductive Adhesive with High Performances

Mingkun Yang, Yongjun Huo, *et al.*

MARCH 15, 2023
ACS APPLIED POLYMER MATERIALS

READ 

Get More Suggestions >